Influence of residual stresses on the fatigue life of welded joints. Numerical simulation and experimental tests

Andrea Chiocca [a],*, Francesco Frendo [a], Francesco Aiello [b], Leonardo Bertini [a]

[a] *Department of Civil and Industrial Engineering, University of Pisa, Pisa, Italy*
[b] *Department of Mechanical Engineering, Eindhoven University of Technology, Eindhoven, The Netherlands*

ARTICLE INFO

ABSTRACT

Residual stresses constitute an inevitable consequence of the most ordinary manufacturing processes, leading to high and not easily foreseeable stress field within a component. Fatigue design codes typically address residual stresses by means of very conservative assumptions, which may results in poorly optimized designs and unexpected failures. Nowadays, the increasing motivation towards an optimized material application require a more reliable fatigue assessment of welded joints and residual stress evaluation. This study investigates the influence of residual stresses on the fatigue assessment of a S355JR structural steel pipe-to-plate welded joint subjected to fully-reversed torsional and bending loading. Influencing factors, such as geometric discontinuities and the material heterogeneous microstructure were considered through numerical modelling and microstructural analysis respectively. Firstly, an uncoupled thermal–structural finite element simulation was carried out to assess the complete residual stress field within the specimen generated by a gas metal arc welding process. Both thermal and structural simulations were developed to achieve an optimal trade-off between simulation time and results accuracy. Then, residual stresses were mapped and included as initial condition in numerical models intended for fatigue damage factors calculation. Fatigue analysis was conducted by means of the Fatemi–Socie critical plane factor and the hydrostatic stress as local damage parameters. Experimental results were then used to corroborate numerical models and verify their capability in assessing the fatigue endurance. Both the experimental data and the applied damage factors have shown an effect of residual stresses on the fatigue life of welded joints when torsional loading was applied. Data further agreed that no influence of residual stresses was detected in the case of bending loading.

1. Introduction

Welding is one of the most widespread production processes used to join metal components. The large adoption of welding is due to all the advantages that this process provides, such as design flexibility, ease to use into automatic production process, weight-saving and cost-saving. Unfortunately, welding also presents disadvantages which can, in some cases, preclude its application. Some of the most common issues include misalignment [1], ease of fracture [2], reduction of buckling resistance [3], reduction of the fatigue life [4] and generation of high tensile residual stresses [5]. Most of the above mentioned problems are caused by the highly localized heat generated in a defined volume which leads to non-linear expansions and contractions of the material causing high plastic deformations. With respect to all issues that may occur, residual stresses are of particular importance as they can strongly affect the durability of a component [6,7] (i.e. both the

static and fatigue strength), playing a key role in modifying crack nucleation and propagation nearby the weld bead. Furthermore, the difficult assessment of residual stresses and their high variability with regard to joint geometry, material and process parameters, makes this subject challenging. Residual stresses may have different consequences on the component life depending on whether they are tensile or compressive. Tensile residual stresses can lead to unexpected component failures as they increase stresses in critical locations. On the contrary, compressive residual stresses can be beneficial and are often sought after since they may bring benefits and enhance the fatigue life [8–11].

Several studies have shown a dependency between fatigue life of welded joints and residual stresses. Sepe et al. [12] have identified how in a tube-tube welded joint the post-weld heat treatment increased fatigue life and also changed the failure mode, compared to specimens in as-welded condition. Manai et al. [13] made a probabilistic study of

---

welding residual stresses for several materials and plate thicknesses. They stated that residual stresses, in the weld toe location, strongly affect fatigue life of welded joints. Another example is offered by Ferro et al. [14] which discovered how, in welded components, the increase of weld passes decrease the high cycle fatigue strength.

One factor that must be considered is the inherent variability of residual stresses. This is mainly caused by specimen geometry, process parameters, material and environment, as well as the stress field redistribution after fatigue or static loading application if material plasticity is considered. Another important restriction is related to the impossibility of transferring data from small scale specimen tests, as residual stresses strongly depend on the weld geometry, problem scale and constraints [15].

A problem which, on the other hand, can nowadays be treated more easily is the evaluation of residual stresses themselves. Considering the state of the art (i.e. IIW [16]) residual stresses have been incorporated as fatigue enhancement factors for reference curves by elaborating a large amount of experimental data. What standard codes seek to achieve is generalizing a wide variety of welded components and materials. Unfortunately, when it comes to residual stresses, their high variability connected to materials, process parameters as well as joint geometries requires each case to be considered separately.

The use of experimental tests alone does not allow to determine the entire residual stress field within a component, because of the intrinsic uncertainties of some methods and the high cost and time involved in the measurement. In the last decades, residual stresses evaluation by numerical approaches has become widespread, especially for problem such as casting [17–21], welding [22–34] and additive manufacturing [35–40]. What makes the numerical evaluation of residual stresses challenging is the multiphysics environment involved. Interfacing different simulation environments requires first of all assessing whether the physics are coupled or uncoupled. Another issue to be addressed concerns the determination of temperature-related non linear material properties, (i.e. thermal or structural). It is common practice to use material properties derived from the literature, since their evaluation through experiments is extremely expensive and time-consuming. Moreover, although the structural part of the simulation is rather standard (e.g. through the use of the *element birth & death* technique), the thermal analysis differs for the heat source selected for the simulation. Some of the most commonly implemented thermal heat sources are the Goldak's double ellipsoid [41], Gaussian heat source [42] and volumetric heat flux [24]. They differ mainly in the number of parameters that must be defined and the complexity of numerical implementation. Nevertheless, numerical methods have been recently much more often employed in the evaluation of residual stresses [43,44]. Recent developments in computing methods allowed multiphysics simulations to become increasingly time-efficient and trustworthy, although the combined application of experimental procedures is currently necessary for an accurate validation of numerical results.

In this paper a numerical and experimental analysis is presented regarding the influence of residual stresses on the fatigue life assessment of a pipe-to-plate welded joint made of structural steel S355JR. The work was aimed at determining whether welding residual stresses exhibit an influence on the high-cycle fatigue (HCF) life of a pipe-to-plate welded component, under different loading conditions. The experimental campaign was used to obtain fatigue lives data for the considered loading conditions, for as-welded and stress relieved specimens. At the same time, a complex numerical procedure was developed to obtain the residual stress field inside the component, as a results of the welding procedure. After that, a local stress analysis, based on two local damage parameters, was used to obtain an estimate of he fatigue resistance of the considered joint. This detailed numerical simulation is a research-oriented unconventional procedure and, up to the authors' knowledge, not already discussed in the technical literature. As a matter of fact, thermal–structural analyses for residual stress evaluation are rarely done for this kind of joint, although it is a widely used geometry

within the industry. The most common loads experienced by a pipe-to-plate welded component are torsion and bending. For this reason the present work attempts to highlight whether the residual stress field leads to a component early failure when one of these loading conditions occurs. Additionally, the work wants to independently corroborate, from a fatigue prospective, the recently developed thermal–structural model, presented by the same authors [44–46].

In the first part of the work, the numerical analysis is presented and discussed. Specifically, an uncoupled thermal–structural simulation was firstly solved in order to evaluate residual stresses due to the welding process. The thermal–structural model is somewhat distinct from those presented previously. A Constant Initial Temperature (CIT) heat source model was used during the thermal simulation and a more representative solidification sequence was applied in the structural model together with temperature dependent elastic–plastic material properties [44,45]. Subsequently, an elastic–plastic structural simulation was performed to determine damage due to fatigue loading in as-welded and stress-relieved conditions. Damage factors such as Fatemi–Socie critical plane factor and hydrostatic stress were used to numerically assess the damage due to fatigue loading.

Afterwards, the experimental fatigue assessment is discussed regarding a pipe-to-plate welded joint in as-welded and stress-relieved conditions, under fully reversed (i.e. load ratio $R = -1$) bending and torsion. In addition, the microstructure of the Fusion Zone (FZ), Heat Affected Zone (HAZ) and Base Material (BM) were studied for both As-Welded (AW) and Stress Relieved (SR) conditions, thus to better understand microstructure influence on the fatigue life assessment of the welded joint.

2. Material and methods

The specimen shown in Fig. 1, i.e. a pipe-to-plate welded joint made of S355JR structural steel as base material and EN ISO 14341-A G 464 as filler material, was employed for the investigation. The welding processes involved, firstly, a welding between the pipe and two circular plates, followed by a welding between the pipe and the base quadrangular plate, in both cases by means of a single pass of Gas Metal Arc Welding (GMAW). Specifically, a conventional Metal-arc Active Gas (spray transfer and high voltage) welding was employed using a protective oxidizing gas via a mixture of argon and carbon dioxide. The welding process was carried out manually at room temperature through an Trans Plus Synergic 4000 machine. While the welding torch position was kept steady by the operator, the specimen was rotated through a bench whose angular speed was controlled by the operator. The parameters of the welding process are shown in Table 1 and resulted in a partial penetration weld bead, as shown in Fig. 2. Both base and filler material chemical compositions as well as mechanical properties of the base material are given in Table 2, Table 3 and Table 4, respectively. In Table 4 the following parameters are presented: yield strength $R_{p0.2}$, tensile strength R_m, Young's modulus E, tangential modulus G, Poisson's ratio v and the Vickers microhardness HV_{10}.

All the specimen geometrical parameters, such as inner pipe diameter (44 mm), pipe thickness (10 mm), side length of the quadrangular plate (190 mm), plate thickness (25 mm) and diameter of the holes (21 mm) required to clamp the specimen on the fatigue test bench, are shown in Fig. 1. The holes as well as the inner volume created by the internal circular support (i.e. pressurized chamber of Fig. 1) were employed to fix the specimen on the test bench and to monitor the presence of a through-the-thickness crack during tests, respectively (see e.g. [47–50]).

The specimens were tested under load control by means of 63 kN linear actuators in a frequency range of 5 Hz–10 Hz through a properly developed test-bench, as shown in Fig. 2a. The load was applied to the specimens through a loading arm, connected to two independently controlled hydraulic actuators.
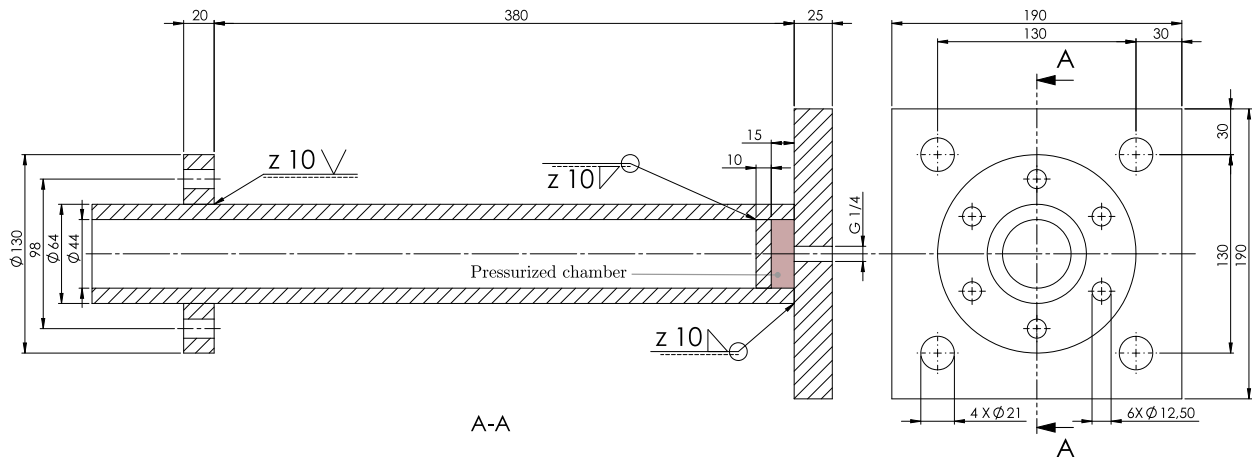
Fig. 1. Technical drawing of the investigated pipe-to-plate welded joint with dimensions in millimetres and welding representation according to ISO 22553:1992.

Table 1
Welding process parameters.

Current (A)	Voltage (V)	Welding Time (s)	Welding Speed (mm s^{-1})
211	25	75	2.7

Filler material	Wire diameter (mm)	Shielding gas	Gas flowrate (m^3 h^{-1})
EN ISO 14341-A G 464	1.20	82% Ar 18% CO_2	0.62

Table 2
Chemical composition (wt%) of S355JR steel (i.e. provided by the supplier company).

C	Si	Mn	P	S	N	Cu
0.24	0.55	1.6	0.035	0.035	0.012	0.55

Table 3
Chemical composition (wt%) of EN ISO 14341-A G 464 filler material (i.e. catalogue values).

C	Si	Mn	Cu
0.065–0.08	0.90–1.00	1.60–1.70	max. 0.30

Table 4
Mechanical properties of S355JR structural steel at room temperature (i.e. provided by the supplier company).

$R_{p0.2}$ (MPa)	R_m (MPa)	E (GPa)	G (GPa)	v	HV_{10}
355	470	206	77.4	0.33	160

Tests were performed under fully reversed ($R = -1$) bending (equal loads on both actuators) and under fully reversed ($R = -1$) torsion (opposite loads on the actuators). Tests were interrupted when a through-the-thickness crack was detected by a pressure drop in the pressurized chamber.

In order to evaluate the influence of residual stress on the fatigue endurance, some specimens were stress relieved before testing; to this aim specimens were heated up to 630 °C with a heating rate of 10.5 °C min^{-1}, held at 630 °C for 4 h and then cooled down, slowly, left in the furnace until room temperature was reached.

A microstructure analysis of the specimens, in particular in the weld seam region, was carried out by micrographs and hardness tests, obtained through an optical microscope Leica DMI3000M and an Akashi AVK-C1 hardness machine, respectively.

3. Numerical analysis

3.1. Thermal–structural analysis

The following section together with Appendix A provide a concise description of the thermal–structural simulation performed, sufficient for a proper understanding of what follows. However, for a complete overview of this section the reader can refer to the following works [44,45], which also include the experimental validation of the thermal–structural numerical model.

Fig. 3 summarizes the simulation steps used to obtain the residual stress state by means of a thermal–structural analysis, which reproduces the thermomechanical response of the material due to the welding process. The analysis has been performed through an uncoupled transient numerical model with temperature dependent elastic–plastic material properties. Thermal and structural simulations have been sequentially solved. The thermal analysis was firstly solved, in which the nodal temperature was the only degree of freedom involved. The analysis is intended to determine the transient thermal profile due to the heat input occurring during the welding process. The heat source used in this case, differs from the classic Goldak models commonly employed in literature; it is a constant initial temperature (CIT) model developed by the same authors and validated in recent works [44,45]. The CIT model is based on a single calibration parameter configurable by comparison with experimental data; it was proved to be an optimal trade-off between accuracy and computation effort. The thermal model simulates the time history of the temperature distribution due to the welding process using the *element birth and death* technique, while activating a fixed number of elements belonging to the weld seam at a constant initial temperature. The volume of activated elements is dependent on the welding speed, which is considered constant in this case. Subsequently, residual stresses and strains have been determined through a structural analysis which employs the previously obtained thermal history as input load. The structural analysis applies the correct solidification sequence of the molten metal belonging to the weld bead by using a macro code implemented in the finite element programme (called *representative welding process* RWP). According to this method, at each load step, only the elements whose nodes have a temperature lower than the melting temperature are activated. The numerical model was validated by comparing experimental and numerical relaxed strains [44,51]. Results were compared and the sound agreement between numerical and experimental data proved the quality of the model described above.

Fig. 4a shows the results of the complete residual stress field of radial and hoop stresses on the plate surface. The weld root and weld
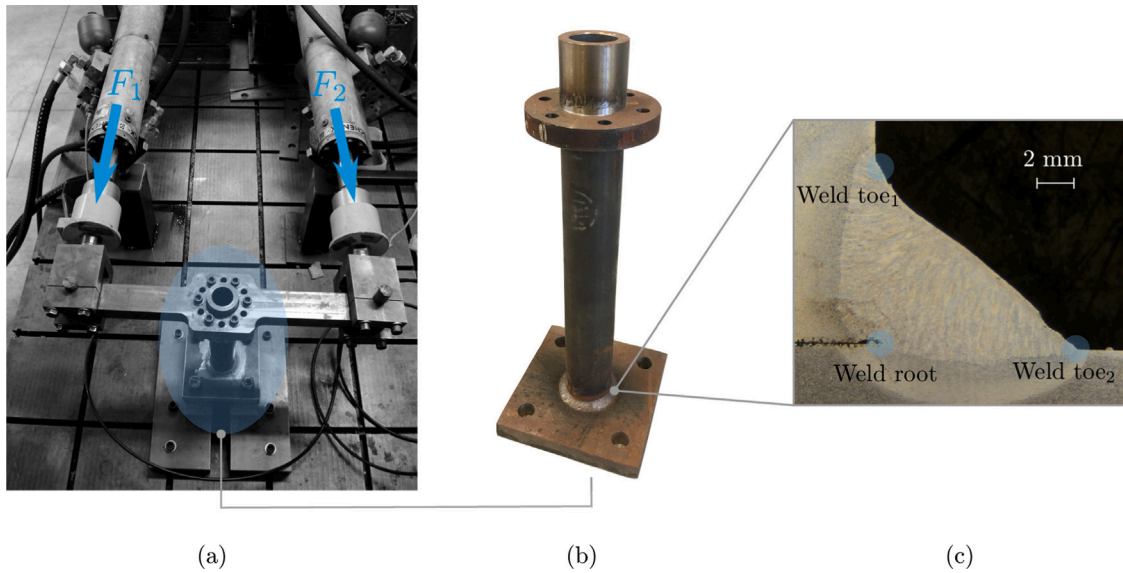
Fig. 2. Test-bench employed for fatigue testing (a), pipe-to-plate welded joint (b) and micrography of the weld seam (c).
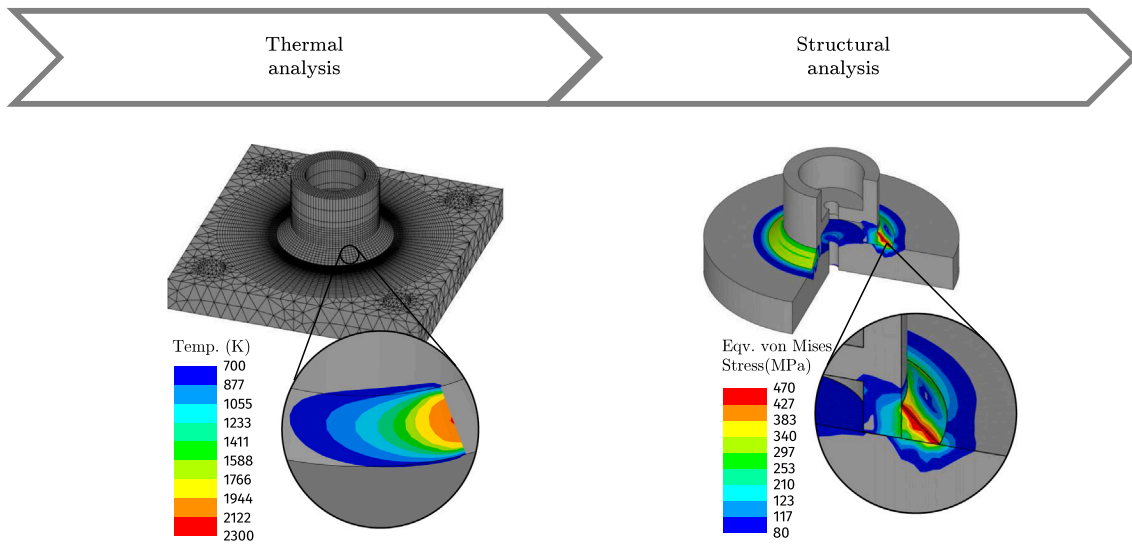

Fig. 3. Flow chart of the uncoupled thermal–structural simulation for residual stresses evaluation in the pipe-to-plate welded joint.

toe have been highlighted through red lines to provide a more accurate representation of the weld seam location. It is worth noting that the entire residual stress field presents an axisymmetric behaviour (i.e. both radial and hoop stresses) except for a restricted area around the run in-run out point. In this particular location, the double thermal process that the material undergoes gives rise to a loss of symmetry in the stress field. Fig. 4b shows a cross-sectional plot of radial and hoop stress away from the run in-run out location (i.e. 180°). Also in this case weld toe and weld root locations are graphically denoted by red lines.

3.2. Fatigue analysis

The fatigue analysis consists of two main parts: a linear-elastic analysis of the entire component subjected to bending or to torsion and a local elastic–plastic analysis, carried out by a submodel. The initial linear-elastic analysis was used to obtain the nodal displacements on the boundary regions of the submodel; besides, to distinguish between as-welded and stress relieved conditions, residual stresses have been initialized in the submodel for the as-welded case, while the initialization phase was skipped otherwise.

As shown in Fig. 5a, the imposed boundary conditions were two remote forces (i.e. used to simulate the actuators load) and four bolt constraints at the interface between the plate and the crankcase. Both remote force and bolt constraint surfaces have been established in regions sufficiently far from the submodel interfaces, not to cause any boundary effect on the submodel analysis. The linear elastic FE-model reproduces exactly the structural model already discussed in Section 3.1 and Appendix A. It uses the same mesh pattern and the same element type (i.e. SOLID185), only varying the material properties.

The sub-model geometry (Fig. 5b) was defined by means of a sensitivity analysis to ensure a negligible influence of the boundary surfaces on the stress and strain results.[1] The submodel includes the actual fillet radii measured starting from a cross section of the real weld, thus providing a more representative stress gradient at the notches (i.e. 0.2 mm of notch radius for the weld root and weld toe belonging to

---

[1] The sensitivity analysis was carried out on nodes belonging to weld root and weld toes, varying the submodel extension angle until no influence on results was exhibited.
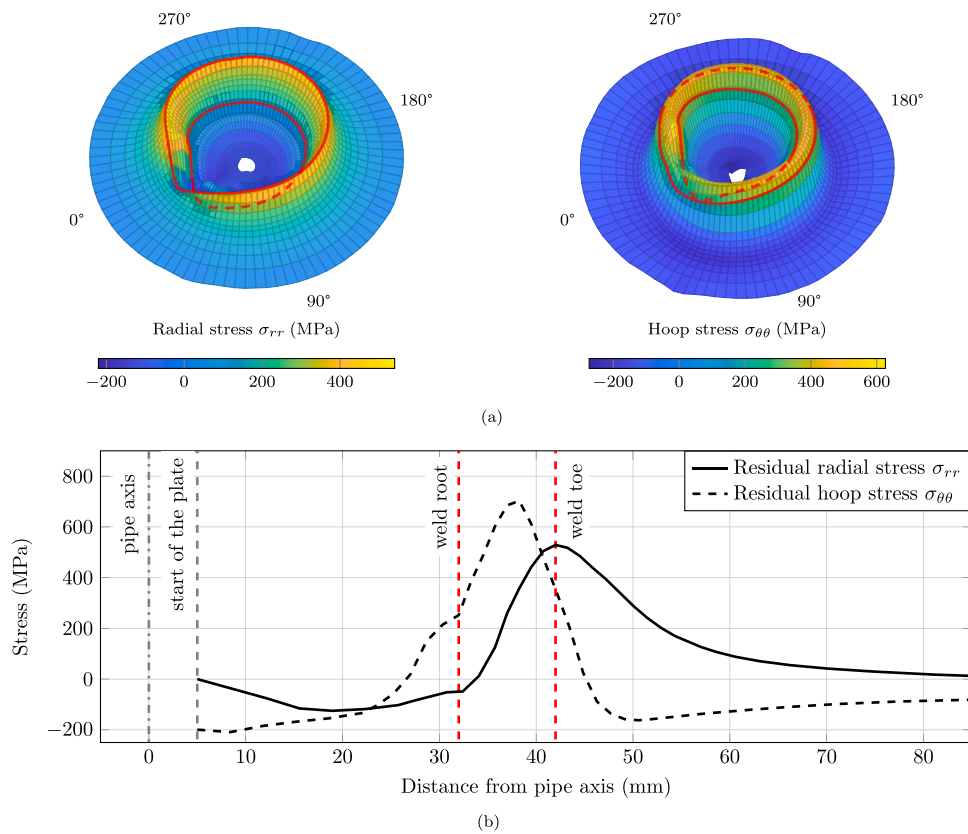
Fig. 4. Radial and hoop residual stress on the plate surface with indication of the angular coordinate (i.e. run in-run out point at 0°) and weld bead deposition area (i.e. between red lines) (a). Cross sectional plot of residual stress distribution on the plate surface at an angle of 180° from the run in-run out point (b).
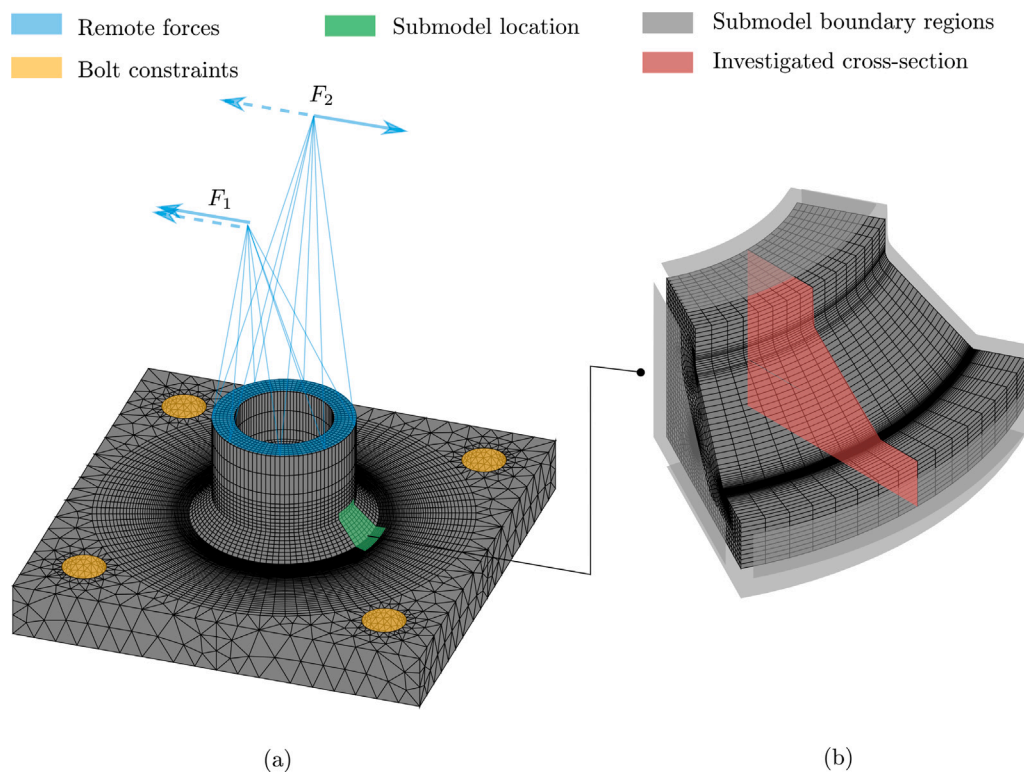

Fig. 5. Finite element models for the linear-elastic analysis (a) and elastic–plastic submodel analysis for fatigue damage parameters evaluation (b).
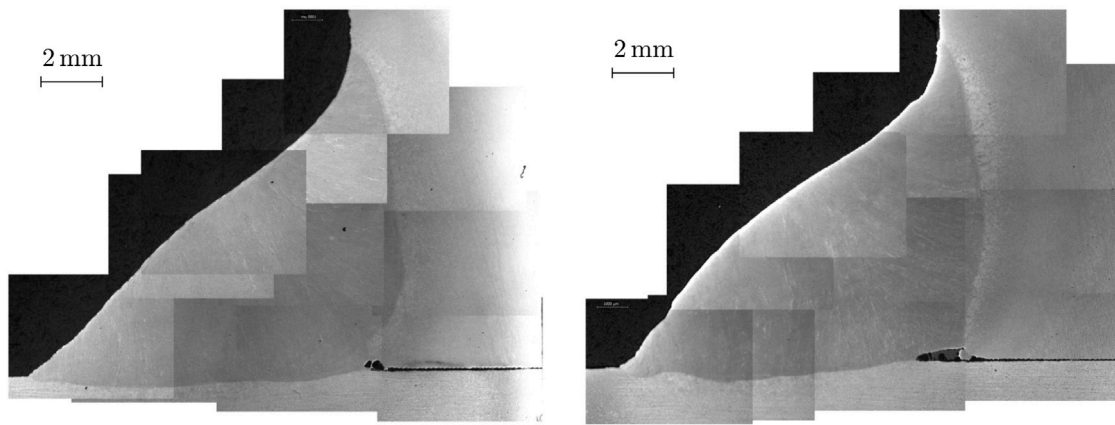
Fig. 6. Examples of cross sections of the weld bead.

the base plate and 1 mm of notch radius for the remaining weld toe). It should be noted that geometric variability is inherent in the welding process. The examined weld toe and weld root radii have shown large dimensional variations. Especially for the weld root, which was experimentally found to be critical for crack initiation, it is sometimes difficult to define even a radius. Within the definition of the numerical model, the smallest radius measured was cautiously taken. Fig. 6 shows the heterogeneity of the bead readings and demonstrates the difficulty in finding a single measurement to introduce into the numerical model.

Elastic–plastic cyclic material properties were implemented in Ansys© through a multi-linear isotropic hardening material model with stress–strain curve obtained from [52]. The material properties used here refer to a cyclically stabilized curve, as the component was assumed to have been already exposed to a significant number of cycles. The FE-model was characterized by a really fine mesh in all notch regions with an average element size of 0.05 mm in the weld root and weld toes and an average element size of 1 mm everywhere else. The submodel had a total number of 155454 nodes and 35408 elements. Considering the complex state of stress at the critical locations, it was decided to use a damage parameter that can quantitatively describe the stress triaxiality and consider the material plasticity, as well. All approaches to damage described in the following are based on assumptions of local and continuous mechanics.

Based on the above considerations two damage parameters were used. The first one was based on the critical plane concept of *Fatemi–Socie*, as defined by the following relationship:

$$FS = \frac{\Delta\gamma}{2}\left(1 + k_{FS}\frac{\sigma_n}{S_y}\right) \tag{1}$$

where k_{FS} is the material parameter. $\Delta\gamma$ is the shear strain range, σ_n is the normal stress acting on the critical plane and S_y is the material yield strength.

Experimental data were interpreted by means of the FE-model shown in the Fig. 5b, calculating the planes that experience the maximum value of FS. A ductile material parameter have been adopted, $k_{FS} = 0.4$, in the same way as [53]. As a matter of fact, *Fatemi–Socie* critical plane factor is usually employed for ductile materials and in proportional loading cases [54].

Critical plane factors were evaluated relatively to the cross-section of Fig. 5b, which represent the most stressed area during bending loading; on the contrary, a uniform stress distribution along circumferential direction is expected under torsion loading. Critical plane factors were computed by implementing Eq. (1) in a Matlab© code. The as-welded condition was obtained by mapping residual stresses from the thermal–structural model described in Section 3.1. In order to optimize the computation time, the critical plane code was run solely for the nodes belonging to the weld notches. The crack nucleation plane can be predicted by directly applying Eq. (1) for all combinations of angles that define the spatial location of the critical plane.

The second damage parameter used was the hydrostatic stress. The hydrostatic stress is, de facto, the mean value computed over the normal stresses acting on an infinitesimal volume of material (i.e. nodes of the finite element model in our case) and is mainly responsible for the volumetric changes in the part. This parameter is useful to assess the fatigue life of a torsionally loaded component [55,56]. Hydrostatic stress is directly linked with stress triaxiality that, especially for notched components, plays an major role in the ductile fracture of metals [57]. It has been shown by the work of Crossland [58] and subsequently Burns et al. [59] that a superimposed large hydrostatic pressure has a significant effect on torsional fatigue life since a large compressive normal stress component is introduced in the planes of maximum tangential alternating stress.

4. Experimental analyses

4.1. Fatigue analysis

All specimens have been tested through the test bench already presented in Section 2.

Cracks always initiated from the weld root for pure torsion and mainly from the root, with, occasionally, very few failures originated from the weld toe on the plate side, under pure bending loading.[2] All data used in this work (i.e. reported in Tables B.5 and B.6 of Appendix B) refer to specimens that failed starting from the weld root. The weld root represents, indeed, the region where the highest stress intensification occurs and, as illustrated in [50], where the highest damage parameters were found. Two typical example of the failure surfaces obtained under fatigue bending and torsion loading are shown in Figs. 7–8.

Fig. 7a–b shows a typical fracture surface developed by mode I fracture, both locally and globally. There is usually a single (or few) crack initiation point (i.e. in the most stressed area) from which the crack tends to propagate fairly quickly, showing no degree of interlocking. On the contrary, Fig. 8a–b shows a typical *factory roof* crack propagation pattern with multiple fracture initiation points and frequent plane transitions (i.e. cracks alternate between planes at maximum normal stress). Cracks grow via mode III globally and mode I only locally, showing a high degree of interlocking which decreases the crack propagation rate. It is worth noting that, no significant differences were observed in the macroscopic morphology of the fracture surface, between the as-welded and stress relieved specimens.

---

[2] The variability in the starting crack location can be attributed to the inherent variability of welds geometry.

Fig. 7. Fractured surfaces from bending loading: plate view (a) and pipe view (b); some of the crack starting locations have been highlighted by red arrows.

Fig. 8. Fractured surfaces from torsional loading: plate view (a) and pipe view (b); some of the crack starting locations have been highlighted by red arrows.
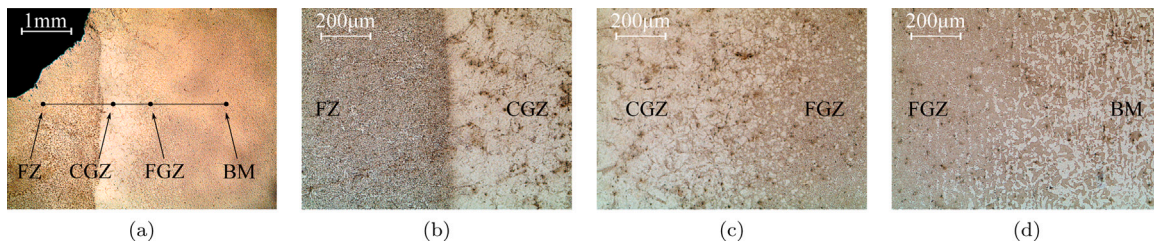

Fig. 9. Optical microscope micrograph of the joint in AW condition. Focus on the weld toe showing fusion zone FZ, coarse grain zone CGZ, fine grain zone FGZ and base material BM (a). Detail of the microstructure transition between FZ and CGZ (b), CGZ and FGZ (c), FGZ and BM (d).

4.2. Microstructure analysis

The heat treatment influence on the microstructure and mechanical properties was analysed through microstructural analyses and hardness measurements. Two samples were employed for this. One sample was extracted from the weld bead of the as-welded (AW) and one from the weld bead of the stress relieved (SR) joint. Both samples were extracted far from the crack initiation point. The samples were obtained through cuts made on a plane containing the pipe axis. The samples were incorporated in a thermosetting resin, grounded using SiC waterproof papers with grits of 120, 320, 500, 800 and 1200, then mirror-polished using diamond paste. In order to highlight the microstructure, they were etched with Nital reagent (2%). Samples were observed by Leica DMI3000 M optical microscope. Micro hardness measurements were performed according to ASTM E92-17 [60] using the approximate test force of 10kgf. The measurements were performed along a line orthogonal to the bisector of the bead angle.

Fig. 9 shows the optical microscope micrograph of the joint in AW condition. Fig. 9a focuses on the weld toe showing four main areas produced by welding. According to the denominations used in the scientific literature [61–63] they have been named: Fusion Zone (FZ), Coarse Grain Zone (CGZ), Fine Grain Zone (FGZ) and Base Material (BM). The FZ is the region formed by the solidification of the filler metal while the BM is the region of the joint material that has kept its microstructural characteristics unchanged during the welding process. The portion of material between BM and FZ during welding undergoes a heat process that alters its original microstructure. This zone is generically referred to as the Heat Affected Zone (HAZ). The portion of the HAZ closest to the FM is subjected to high temperature values, close to the melting temperature of the steel. The long stay at high temperature makes the austenite grain coarser forming the CGZ [64]. Conversely, the portion of HAZ closest to the BM is subjected to lower temperature values and short dwell times, producing fine prior austenite grain [65] forming the FGZ. Fig. 9(b-d) show the microstructural variation of the bead progressively moving away from the FZ.
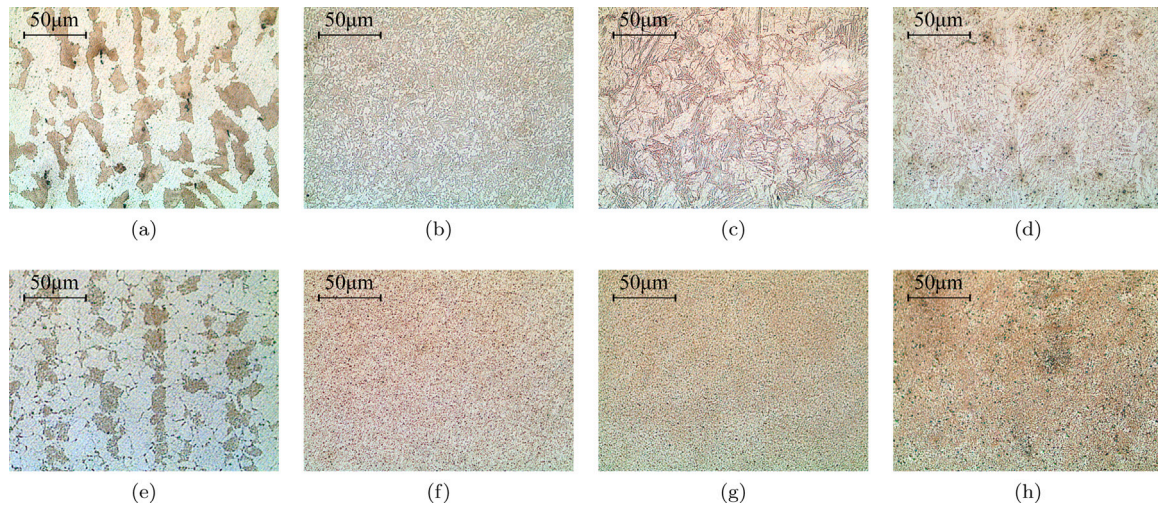
Fig. 10. Optical microscope micrograph showing the microstructures of the BM (a), FGZ (b), CGZ (c) and FZ (d) of the joint in the AW condition. (e-h) show the corresponding microstructures of the joint in the SR condition.
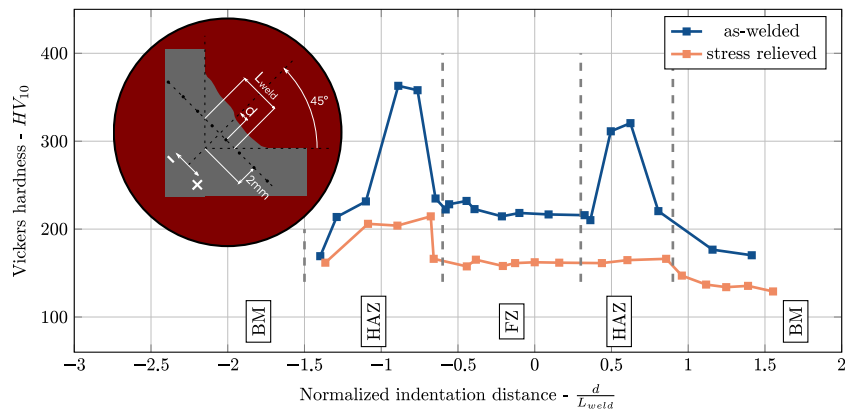

Fig. 11. Vickers hardness distribution around the weld toe in as-welded and stress relieved conditions.

Fig. 10(a-d) show in detail the microstructure of the four zones described above. Fig. 10a shows the microstructure of the BM characterized by perlite islands surrounded by proeutectoid ferrite (white phase). Fig. 10b shows the microstructure of the FGZ, it appears uniform with very fine grain showing characteristics typical of a martensitic or bainitic microstructure. The microstructures of the CGZ (Fig. 10c) are characterized by the presence of pearlitic colonies with small ferrite islands. Similarly, the microstructure of the FZ (Fig. 10d) is uniformly distributed perlite.

Fig. 10(e-h) show the corresponding microstructures of the joint in the SR condition, obtained in the same position as the previous ones. The BM Fig. 10e did not undergo microstructural changes following the thermal process, its microstructure remained the same as that of the BM in the AW condition. However, the microstructures obtained in the HAZ and FZ of the joint in the SR condition (Fig. 10(f-h)) are similar among each other and significantly different from those in the AW condition. The Fe_3C layers present in the perlite have lost their lamellar shape and appear uniformly distributed in the ferritic matrix [66].

Metallographic analysis were carried out both in proximity and away from the *run in-run out* region[3] showing no significant differences. Fig. 11 shows the comparison between the hardness distribution around the weld toe in AW and SR condition.

The graph shows a diagram of the weld bead which defines the reference system adopted, the weld length L_{weld} and the indentation distance d. The normalized indentation distance d/L_{weld} is reported on the abscissa axis and the Vickers hardness on the ordinate axis (HV_{10}). It should be noted that the ordinate scale does not start from zero but is such as to highlight differences between the examined samples. In the hardness profile of the joint in AW condition, the FZ assumes an uniform hardness value equal to 230HV. The maximum value obtained is 370HV in correspondence with the FGZ portion of the HAZ, where the material has a finer microstructure. The hardness profile of the joint in the SR condition appears uniform assuming hardness value equal to 170HV in the region of FZ and HAZ while it decreases slightly in the BM area. The heat treatment has overall reduced the hardness of the steel uniforming it along the entire joint. The high hardness values obtained in the FGZ have undergone a variation ΔH of about 170HV. Considering the percentage of carbon and of the alloying elements reported in Table 2 the value obtained is in accordance with the traditional theory which expresses the hardness of martensite after tempering at 630° for 4h [67,68]. The results obtained from the metallographic and hardness analysis were found to be in agreement with the results of the literature for subcritical annealing treatments. Therefore, the thermal process employed is expected to provide a sufficient reduction of residual stresses in order to produce an appreciable effect on the component fatigue life.
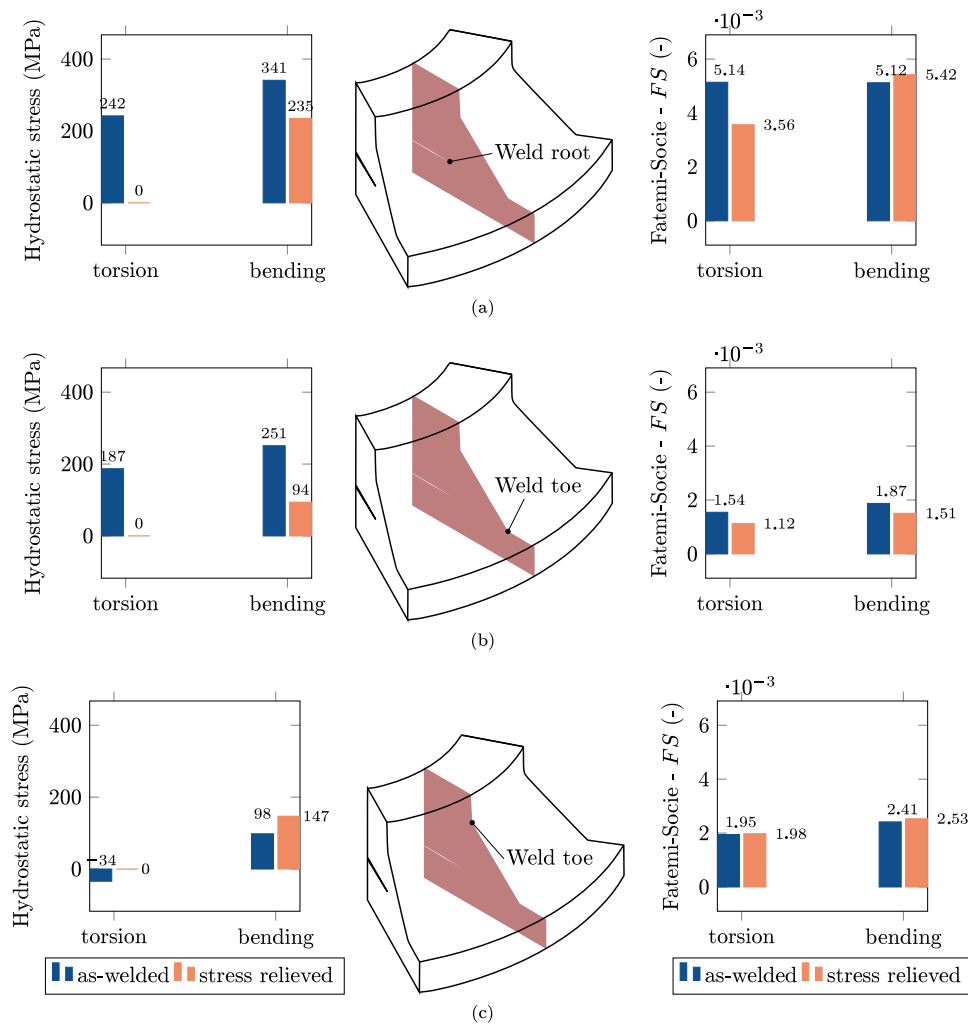
---

[3] The *run in-run out* is the region in which there is simultaneously the beginning and the end of the welding process.

Fig. 12. Pure bending and pure torsion hydrostatic stress and Fatemi–Socie critical plane factor in the weld root (a) and weld toes (b), (c); hydrostatic stress and critical plane factor values are related to a nominal stress range of 143 MPa in bending and 250 MPa in torsion.

5. Results and discussion

5.1. Numerical results

A preliminary analysis was performed to identify the specimen critical notch in order to perform the subsequent fatigue numerical study. Hydrostatic stress and the *Fatemi–Socie* critical plane factor were used as damage factors for the analysis. Both damage parameters employed belong to the broader category of local damage parameters extensively used in fatigue analysis [69–72].

Fig. 12 shows the hydrostatic stress and *Fatemi–Socie* critical plane factor for different loading and heat treatment conditions. All the values shown in the Fig. 12 represent the maximum value of the damage parameter calculated over the nodal set belonging to the selected weld notch. It is visible that under pure bending the difference in damage between as-welded and stress-relieved states is smaller if compared to the case of torsional loading. A possible explanation for that involves the type of loading. In the presence of pure bending, residual stresses undergoes plastic relaxation during the first loading cycles leading to a stress redistribution that results in similar hydrostatic and deviatoric stress tensor components for the AW and SR states. The opposite is true in the case of pure torsion. In this case the load has less influence (i.e. ideally no influence) on the hydrostatic component, whereas for the AW specimen, due to residual stresses, a significant hydrostatic stress component may be present after specimen loading.

When hydrostatic stress is considered, the weld root appears as the critical notch showing an higher difference between AW and SR cases when it comes to the torsional loading.

Likewise, *FS* critical plane factor identifies the weld root as the critical notch and shows the characteristic difference between torsional and bending load under different heat treatment conditions. It is possible to identify from Fig. 12 how the *FS* damage factor reports the highest values within the weld root, showing a significant difference between AW and SR conditions only in case torsional loading condition. Subsequently, the damage resulting from different loading conditions in AW and SR states was evaluated by directly comparing the maximum values of the critical plane factors as a function of the applied nominal stress range. It should be noted that in the following, only measurements involving the weld root will be reported, as it was identified before as critical notch. The analysis has been carried out with respect to pure bending, as shown in Fig. 13, and with respect to pure torsion, as shown in Fig. 14. The graphs provide results for the Fatemi–Socie critical plane factor over the nominal stress range. The relative difference between the AW and SR conditions (scale on the right vertical axis) has also been reported. The relative difference reaches a maximum value of 8.3% in pure bending for a nominal stress range of 108 MPa–191 MPa, while it goes up to 41.1% in pure
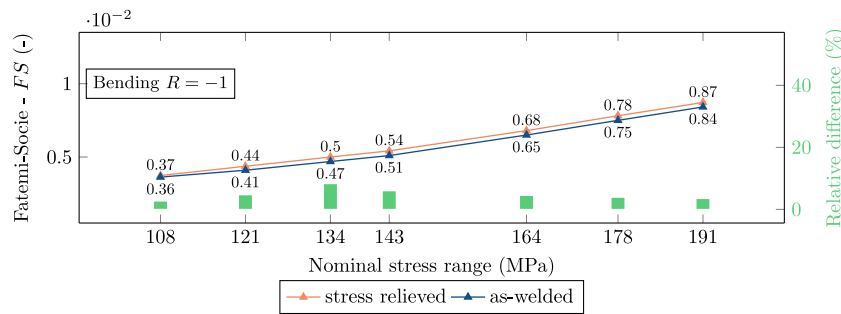
Fig. 13. Fatemi–Socie critical plane factor over nominal stress range under pure bending for a load ratio $R = -1$.
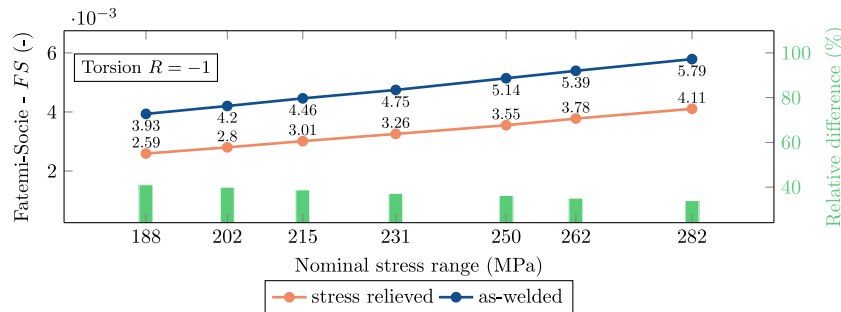

Fig. 14. Fatemi–Socie critical plane factor over nominal stress range under pure torsion for a load ratio $R = -1$.

torsion for a nominal stress range of $188\,\text{MPa}$–$282\,\text{MPa}$.[4] The relative difference never exceeds 10% for the case of bending loading, while it always exceeds 20% for the case of torsion loading. It should be noted that the quasi-linear behaviour obtained in Figs. 13 and 14 results as the material stabilized after the initial fatigue cycles. Actually, critical plane factors were taken as the convergence values obtained during numerical analyses (i.e. convergence was obtained in most cases after few load cycles). It is worth noticing that, critical plane parameters are not representative of the specimen loading condition, which is why the same critical parameter results in clearly different nominal stresses ranges between AW and SR conditions. This can be concluded by looking at Figs. 13 and 14 where the same critical parameter yields different values of nominal stress ranges, particularly in the case of pure torsion.

Fig. 15 presents the endurance curves in terms of critical plane factors vs experimental number of cycle to break-trough. Data of FS over the experimentally evaluated number of cycles to break-trough are shown for all loading and heat treatment conditions. In this case, as the damage factor considered is a local damage parameter, all data were represented on a single plot. Since the calculation of the AW data derived from the implementation of the numerical thermal–structural model, uncertainty in the damage factor calculation could arise. For this reason, solely the fitting of the SR points was reported and used for the evaluation of the *expected vs. experimental number of cycles to break-through* graph as it was considered to be representative for the whole distribution. It can be observed that no clear distinction between pure torsion loading and pure bending loading exists as occurred under nominal stresses, as later discussed in section. This is mainly caused by the local definition of the damage parameter, which accounts not only for the loading condition but also for the local geometry of the component as well as residual stresses.

5.2. Experimental results

Figs. 16 and 17 show the fatigue endurance of both as-welded and stress relieved specimens for pure bending and pure torsion loading, in terms of nominal stress range ($\Delta\sigma_n$) vs. number of cycles to break-through (N_f). Slope coefficients of $K = 5.2$, $K = 7.4$ and nominal stress ranges at 10^6 cycles of 129.4 MPa, 199.7 MPa were obtained for a survival probability of 50% ($P_{50\%}$) for bending and torsion loading cases in the AW condition, respectively. While in the case of SR specimens $K = 3.14$, $K = 9.4$ and nominal stress ranges at 10^6 cycles of 109.1 MPa, 264.5 MPa were obtained for a survival probability of 50% ($P_{50\%}$) for bending and torsion loading cases respectively. The scatter band T_σ reduces from $T_\sigma = 1 : 1.6$ to $T_\sigma = 1 : 1.1$ in pure bending case, and from $T_\sigma = 1 : 1.19$ to $T_\sigma = 1 : 1.13$ if torsion is considered. The scatter band T_σ is defined as the ratio between stresses on the $P_{10\%}$ curve against the $P_{90\%}$ curve, specifically referred to a survival probability of 10% and 90%.

It can be clearly observed that residual stresses lead to a significantly different outcomes under the two load scenarios. In particular, data obtained for SR specimens subjected to pure torsion exhibit an increased in fatigue life by a factor bigger than four if compared to the torsion as-welded data. On the contrary, no appreciable difference can be noticed for the specimens loaded in bending, as all results lie within the same scatter-band. Another experimental evidence resulting from Figs. 16 and 17 is that results of SR specimens show a significant reduced dispersion. This occurs both in bending and in torsion.

For comparison purposes, FAT curves (i.e. with a p.s. of 97.7%) relative to steel welded joints have been presented in both Figs. 16 and 17. The threshold curve for bending (i.e. FAT50/3) refers to IIW fatigue recommendation [16] regarding the structural detail no. 913 loaded in traction. All results fall on the conservative side. The experimental slope of the curve is higher than the one from [16] for AW data, while a similar slope can be found for SR specimens. In the case of pure torsion, a FAT80/5 is suggested for the fatigue resistance of partial penetration welded joints on the basis of shear stresses. In order to report all data on a $\Delta\sigma_n$ vs. N_f plane a resolved FAT curve was derived by multiplying the IIW curve by a factor of $\sqrt{3}$. In this case too, all the results lie on the conservative side of the plane, while FAT curve presents a greater

---

[4] The adopted nominal stress ranges for bending and torsion were chosen to be consistent with the experimental fatigue behaviour of the specimens in as-welded conditions. Both stress ranges yield to an experimental fatigue life range 10^5–10^6.
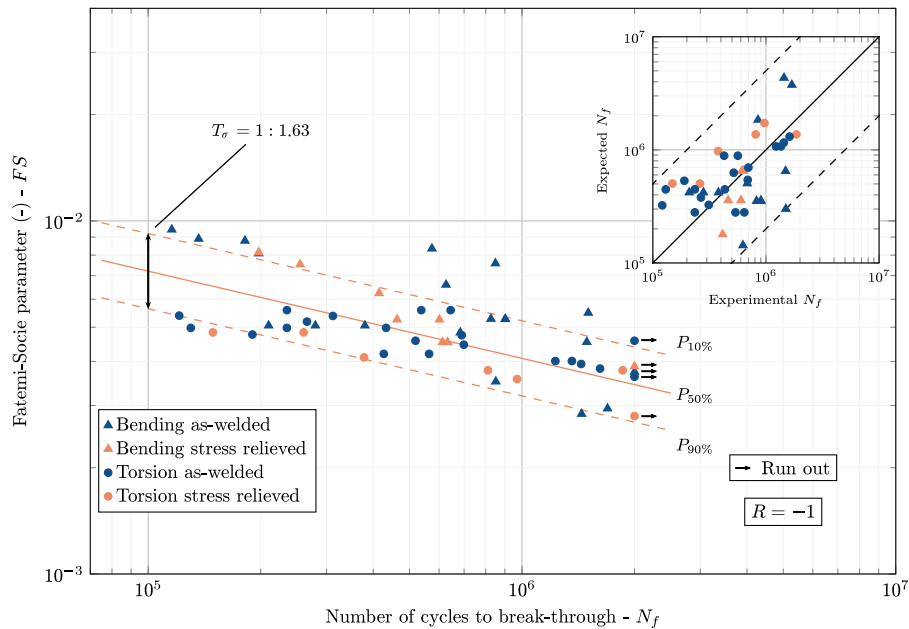
Fig. 15. Fatemi–Socie critical plane factor over the number of cycles to break-through for pure bending and pure torsion loading in as-welded and stress relieved conditions.
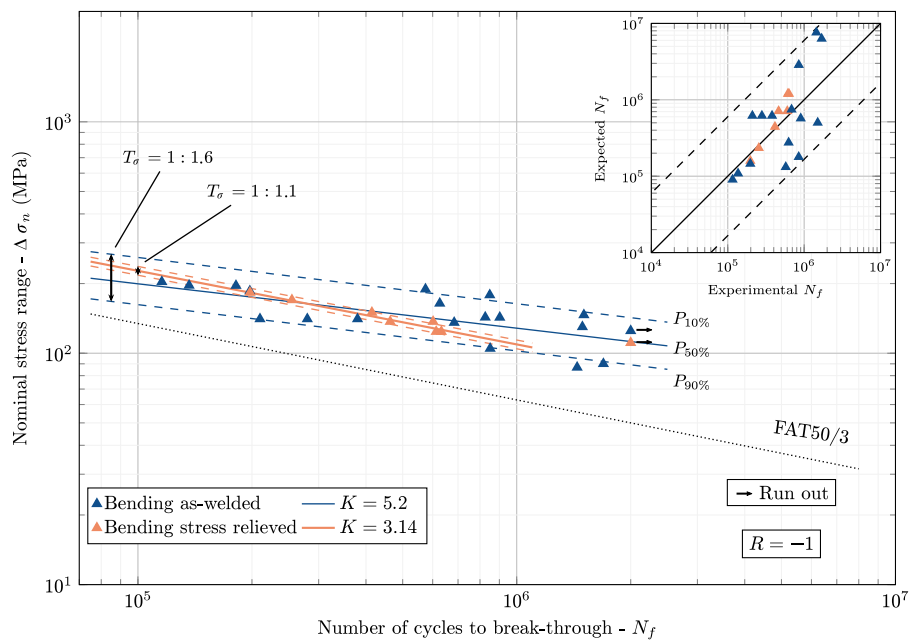

Fig. 16. Nominal stress range over number of cycles to break-through for pure bending loading in as-welded and stress relieved conditions; expected vs. experimental number of cycles to break-through are displayed in the top right corner of the figure.

slope if compared with AW and SR specimens experimental data. It is worth noting that a unit fatigue enhance factor ($f(R) = 1$) was used following the IIW guidelines in the case of three-dimensional welded components.

In the upper right corner of the Figures, the *expected vs. experimental number of cycles to break-through* graph has also been reported. All data point were derived with respect to torsion and bending power-laws in AW condition. Similar consideration can be drawn also in this case. Stress relieved specimens loaded in torsion exhibited an experimental endurance significantly longer than the ones in the AW condition. Indeed, it can be observed that all SR torsion data fall outside the factor three life scatter-range that encompasses all AW torsion data. On the contrary, for bending data, no noticeable difference between SR and

AW can be observed. Specifically, all points fall within a factor six life scatter-range.

6. Conclusions

In the present work the effect of residual stresses on the fatigue life of a pipe-to-plate welded joint, subject to different type of loading, was investigated. Experimental results of nominal stress range over number of cycles to break-trough were obtained and discussed on the basis of numerical data, considering both Fatemi–Socie critical plane factor and the hydrostatic stress. Conventional standard codes do not give clear guidelines concerning the effect of residual stresses on the fatigue life of welded components when considering the load type. The following
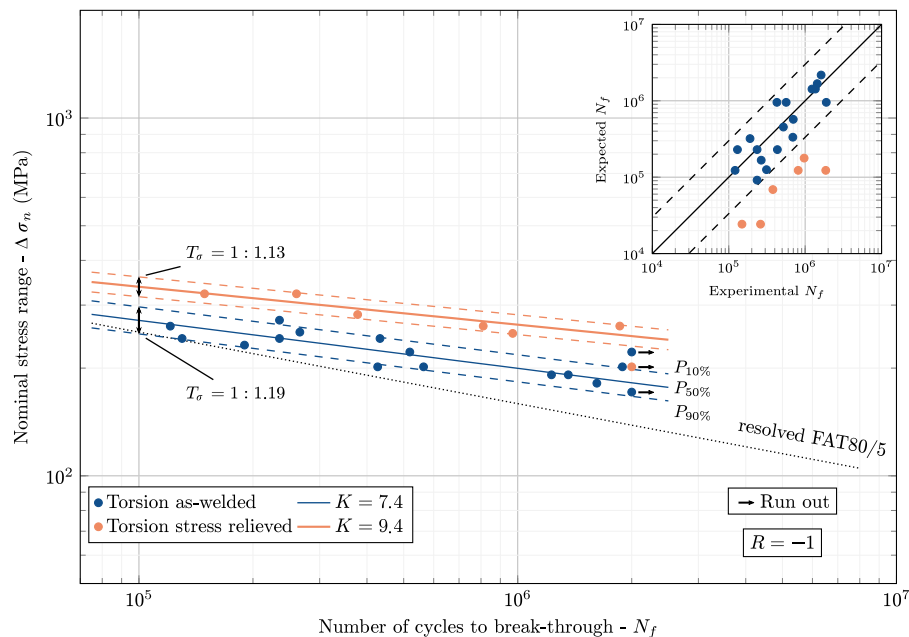
Fig. 17. Nominal stress range over number of cycles to break-through for pure torsion loading in as-welded and stress relieved conditions; expected vs. experimental number of cycles to break-through are displayed in the top right corner of the figure.

results may help to improve knowledge in this area for a tube-to-plate welded component:

- a clear influence of residual stresses on torsionally loaded pipe-to-plate welded joints was found as residual stresses decreased the fatigue life of these components; in this context a stress relieving can lead to improvements in fatigue performance;
- on the other hand, no significant influence of residual stresses was observed for specimens loaded in bending; in this case a stress relieving was observed to provide no significant improvement in fatigue endurance;
- the effect of residual stresses on the fatigue endurance under bending and torsion was successfully explained by both the Fatemi Socie critical plane factor and the hydrostatic stress;
- the hydrostatic stress used as a damage parameter succeeds in describing very well what has been found experimentally; it was observed that the increase in hydrostatic stress between the torsionally loaded SR and AW specimens was well explained by the presence of residual stresses;
- in the same manner the Fatemi–Socie critical plane factor showed an increase in damage for torsionally loaded specimens between SR and AW conditions;
- experimental results obtained with SR specimens appeared to have a significant lower dispersion, if compared to results obtained with AW specimens (i.e. in presence of residual stresses), confirming the fact that residual stresses represent a source of scatter in fatigue lives;
- the thermal–structural model developed by the authors proved to be reliable and to provide effective stress cycles that appeared in agreement with experimental results from a fatigue forecasting standpoint;
- residual stresses are, as matter of fact, a source of uncertainty that introduce complexity in the fatigue assessment of welded joints and complex analysis is required to properly account for them.

Declaration of competing interest

The authors declare that they have no known competing financial interests or personal relationships that could have appeared to influence the work reported in this paper.

Appendix A. Overview of the thermal–structural analysis for residual stress evaluation

This section presents a more detailed explanation of the thermal–structural simulation developed to compute residual stresses due to the welding process.

The entire thermal–structural numerical simulation was performed using Ansys© APDL vers. 19.2 with an eight nodes hexahedral element: a SOLID70 element with nodal temperature as the only degree of freedom was used for the thermal analysis and SOLID185 element with spatial displacements as degrees of freedom (i.e. x, y, z directions) was used for the structural analysis. As shown in Fig. 3, a finer mesh has been used in the weld bead region (i.e. 1 mm), a transition mesh in the heat affected zone (i.e. 1 mm–3 mm) and a coarser mesh everywhere else (i.e. > 3 mm). The FE-model consists of a total of 96420 elements and 97728 nodes. All notches (i.e. weld root and weld toes) have been modelled as perfectly sharp in order to easily simulate the boundary interface between base and weld bead material when using the *element birth & death* technique. Indeed, simulating weld toes and root radii during a thermal–mechanical analysis would have introduced additional issues regarding the convergence of the model, since a dense mesh around notches and a larger simulation time would have been required.

The temperature-dependent thermal and mechanical properties of the material were derived by Zhu et al. [73]. Material properties up to a temperature of 1273 K were implemented in the structural simulation, since no difference was exhibited from implementing properties at higher temperatures. Properties such as Young's modulus, hardening coefficient and initial yield stress reach negligible values for temperatures greater than 1273 K, thereby making their implementation unnecessary. Furthermore, such a simplification improved solution convergence and speed up the simulation. In this case, some phase transformations (i.e. ferrite–austenite), are implicit in the evolution of the thermal properties of the material, while others were not considered in the simulation. However, it has been shown that for low carbon steels, the influence of phase transformations on residual stresses generation is negligible and can therefore be neglected [74–76].

To clarify the steps involved in the thermal–structural simulation, a flow chart is presented in Fig. A.18. The weld bead generation process

1.1) Experimental temperature measurements

The initial temperature T_i is calculated by comparing temperature vs. time results between the thermal analysis and thermocouple measurements obtained during the welding process

1.2) Thermal analysis

The steps to apply the *Constant Initial Temperature* (CIT) method used to reproduce the temperature-time-history of the welding process at a generic time t_i are as follows:

1. the starting temperature of the entire component is set to room temperature
2. selection of all the elements belonging to the weld seam
3. a constant initial temperature T_i is given to the elements selected at point 2
4. all elements of point 3 are deactivated (KILL command in Ansys)
   4.1. identification of the volume of elements belonging to a given angular span corresponding to a small time interval during the weld deposition process
   4.2. selection of all the elements belonging to the weld portion identified at step 4.1
   4.3. activation of all the selected elements (EALIVE command in Ansys)
   4.4. solution of the entire model
   4.5. time increment (Δt)
   4.6. go to step 4.1 until all elements belonging to the weld bead have been activated
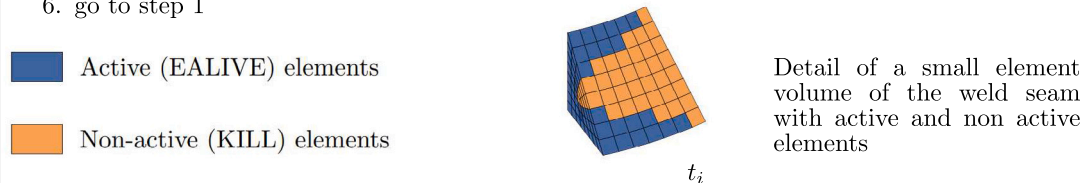5. solution of the entire model until room temperature is reached

Active (EALIVE) elements

Non-active (KILL) elements

Detail of the weld seam

t_i $t_i + \Delta t$
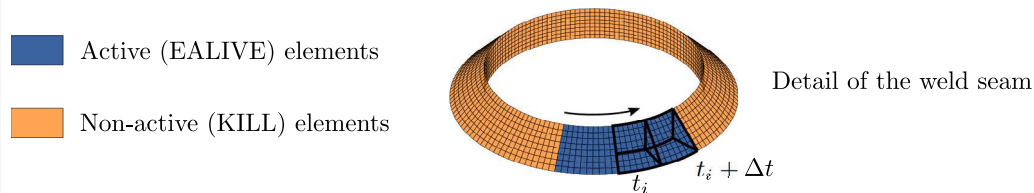
2) Structural analysis

All nodal temperature results from the thermal simulation are mapped and provided to the structural simulation.

Iteration of the *Representative Welding Process* RWP methodology at a generic time t_i during the welding process:

1. selection of all the elements belonging to the weld seam
2. selection of all the elements belonging to the weld portion generated at current time t_i
   2.1. activation of all the selected elements
   2.2. detection of the nodes with temperature above the melting point
   2.3. selection of the elements, with all the nodes belonging to the nodal set selected at 2.2
   2.4. deactivation of elements selected at 2.3
3. selection of all model's elements
4. solution of the entire model at the current time t_i
5. time increment (Δt)
6. go to step 1

Active (EALIVE) elements

Non-active (KILL) elements

Detail of a small element volume of the weld seam with active and non active elements

t_i

3) Experimental validation of thermal-structural simulation

Relaxed radial strain results were compared between the numerical model and experimental tests after incremental drilling the bottom of the base plate

Fig. A.18. Flowchart representing the entire numerical and experimental processes involved in the development of the thermal–structural simulation.

was reproduced by means of a thermal simulation supported by experimental temperature measurements (blocks 1.1 and 1.2 of Fig. A.18) in order to define the initial temperature parameter T_i. Subsequently, a structural simulation was carried out (block 2 of Fig. A.18). The structural simulation was characterized by several transient structural simulations in which the cooling process of a portion of the weld bead gave rise to residual stresses inside the material. The repetition of this process over the entire weld bead and the subsequent cooling of the whole component till room temperature resulted in the final residual stress field. An experimental comparison was carried out in order to verify the accuracy of the results (block 3 of Fig. A.18). To this aim,

Table B.5

Experimental results of as-welded specimens under pure bending (B) and pure torsion (T) loading (load ratio $R = -1$).

Specimen no.	Load	$\Delta\sigma_n$(MPa)	N ($\times 10^6$)
1	B	141	0.21
2	B	141	0.28
3	B	141	0.38
4	B	105	0.85
5	B	90	1.69
6	B	87	1.44
7	B	179	0.85
8	B	204	0.116
9	B	189	0.574
10	B	196	0.136
11	B	164	0.626
12	B	186	0.197
13	B	146	1.50
14	B	143	0.902
15	B	136	0.684
16	B	125	run out
17	B	130	1.49
18	B	143	0.826
19	B	196	0.182
20	T	202	1.89
21	T	222	0.51
22	T	182	1.62
23	T	202	0.564
24	T	192	1.23
25	T	232	0.190
26	T	202	0.427
27	T	192	1.36
28	T	242	0.130
29	T	242	0.235
30	T	252	0.266
31	T	272	0.235
32	T	171	run out
33	T	222	run out
34	T	262	0.121
35	T	242	0.433

Table B.6

Experimental results of stress relieved specimens under pure bending (B) and pure torsion (T) loading (load ratio $R = -1$).

Specimen no.	Load	$\Delta\sigma_n$(MPa)	N ($\times 10^6$)
1	B	137	0.602
2	B	137	0.463
3	B	124	0.613
4	B	111	run out
5	B	183	0.198
6	B	150	0.414
7	B	170	0.255
8	T	202	run out
9	T	250	0.970
10	T	262	1.86
11	T	282	0.378
12	T	323	0.149
13	T	262	0.810
14	T	323	0.260

relaxed radial strains generated during an incremental drilling process from the bottom of the plate were compared to the numerical model.

In terms of computational cost, the thermal simulation required 20 min of computing time, while the structural simulation required 10 h, with regard four physical cores running parallel and 16 GB of RAM available.

Appendix B. Experimental fatigue data

In the following section the experimental results of the fatigue test campaign are shown in tabular form.

Tables B.5 and B.6 present experimental data related to the as-welded and stress-relieved specimens, respectively. All tested samples belong to four different batches, roughly divided over a four-year period. Results are given in terms of nominal stress range ($\Delta\sigma_n$) and number of cycles to break-through (N_f), where $\Delta\sigma_n$ has different formulation according to the load type involved (i.e. pure bending or pure torsion), as shown in Eq. (B.1).

$$\Delta\sigma_n = \frac{2M_b}{\frac{\pi}{64}(d^4 - d_t^4)}\frac{d}{2} = \frac{2\sqrt{3}M_t}{\frac{\pi}{32}(d^4 - d_t^4)}\frac{d}{2} \tag{B.1}$$

where M_b and M_t are the bending moment and torque respectively, d is the diameter identified by the weld toe on the plate and d_t is the external pipe's diameter.

References

[1] Lillemäe I, Lammi H, Molter L, Remes H. Fatigue strength of welded butt joints in thin and slender specimens. Int J Fatigue 2012;44:98–106. http://dx.doi.org/10.1016/j.ijfatigue.2012.05.009.

[2] Chlup Z, Novotná L, Šiška F, Drdlík D, Hadraba H. Effect of residual stresses to the crack path in alumina/zirconia laminates. J Eur Ceram Soc 2020;40(15):5810–8. http://dx.doi.org/10.1016/j.jeurceramsoc.2020.06.044.

[3] Vila Real PM, Cazeli R, Simoes da Silva L, Santiago A, Piloto P. The effect of residual stresses in the lateral-torsional buckling of steel I-beams at elevated temperature. J Construct Steel Res 2004;60(3–5):783–93. http://dx.doi.org/10.1016/S0143-974X(03)00143-3.

[4] Barsoum Z, Barsoum I. Residual stress effects on fatigue life of welded structures using LEFM. Eng Fail Anal 2009;16(1):449–67. http://dx.doi.org/10.1016/j.engfailanal.2008.06.017.

[5] Le T, Paradowska A, Bradford MA, Liu X, Valipour HR. Residual stresses in welded high-strength steel I-Beams. J Construct Steel Res 2020;167:105849. http://dx.doi.org/10.1016/j.jcsr.2019.105849.

[6] Sonsino CM. Effect of residual stresses on the fatigue behaviour of welded joints depending on loading conditions and weld geometry. Int J Fatigue 2009;31(1):88–101. http://dx.doi.org/10.1016/j.ijfatigue.2008.02.015.

[7] Lopez-Jauregi A, Esnaola JA, Ulacia I, Urrutibeascoa I, Madariaga A. Fatigue analysis of multipass welded joints considering residual stresses. Int J Fatigue 2015;79:75–85. http://dx.doi.org/10.1016/j.ijfatigue.2015.04.013.

[8] Bartolozzi R, Frendo F. Stiffness and strength aspects in the design of automotive coil springs for McPherson front suspensions: A case study. Proc Inst Mech Eng D 2011;225(10):1377–91. http://dx.doi.org/10.1177/0954407011403853.

[9] Soyama H, Chighizola CR, Hill MR. Effect of compressive residual stress introduced by cavitation peening and shot peening on the improvement of fatigue strength of stainless steel. J Mater Process Technol 2021;288:116877. http://dx.doi.org/10.1016/j.jmatprotec.2020.116877.

[10] Liu D, Liu D, Guagliano M, Xu X, Fan K, Bagherifard S. Contribution of ultrasonic surface rolling process to the fatigue properties of TB8 alloy with body-centered cubic structure. J Mater Sci Technol 2021;61:63–74. http://dx.doi.org/10.1016/j.jmst.2020.05.047.

[11] Song M, Wu L, Liu J, Hu Y. Effects of laser cladding on crack resistance improvement for aluminum alloy used in aircraft skin. Opt Laser Technol 2021;133:106531. http://dx.doi.org/10.1016/j.optlastec.2020.106531.

[12] Sepe R, Wiebesiek J, Sonsino CM. Numerical and experimental validation of residual stresses of laser-welded joints and their influence on the fatigue behaviour. Fatigue Fract Eng Mater Struct 2020;43(6):1126–41. http://dx.doi.org/10.1111/ffe.13180.

[13] Manai A, Franz von Bock und Polach RU, Al-Emrani M. A probabilistic study of welding residual stresses distribution and their contribution to the fatigue life. Eng Fail Anal 2020;118:104787. http://dx.doi.org/10.1016/j.engfailanal.2020.104787.

[14] Ferro P, Berto F, James NM. Asymptotic residual stress distribution induced by multipass welding processes. Int J Fatigue 2017;101:421–9. http://dx.doi.org/10.1016/j.ijfatigue.2016.11.022.

[15] Friedrich N. Experimental investigation on the influence of welding residual stresses on fatigue for two different weld geometries. Fatigue Fract Eng Mater Struct 2020;43(11):2715–30. http://dx.doi.org/10.1111/ffe.13339.

[16] Hobbacher A. Recommendations for fatigue design of welded joints and components. Tech. rep., International Institute of Welding; 2008.

[17] Sandeep M, Sandeep M. Modeling and analysis of residual stresses in castings using AlSi12(Fe) and NiCu30(Fe) materials. IOP Conf Ser Mater Sci Eng 2020;912(3):032047. http://dx.doi.org/10.1088/1757-899X/912/3/032047.

[18] Jayakrishna P, Chakraborty S, Ganguly S, Talukdar P. A novel method for determining the three dimensional variation of non-linear thermal resistance at the mold-strand interface in billet continuous casting process. Int Commun Heat Mass Transfer 2020;119:104984. http://dx.doi.org/10.1016/j.icheatmasstransfer.2020.104984.

[19] Anglada E, Meléndez A, Obregón A, Villanueva E, Garmendia I. Performance of optimization algorithms in the model fitting of the multi-scale numerical simulation of ductile iron solidification. Metals 2020;10(8):1–18. http://dx.doi.org/10.3390/met10081071.

[20] Ridgeway CD, Gu C, Ripplinger K, Detwiler D, Ji M, Soghrati S, et al. Prediction of location specific mechanical properties of aluminum casting using a new CA-FEA (cellular automaton-finite element analysis) approach. Mater Des 2020;194:108929. http://dx.doi.org/10.1016/j.matdes.2020.108929.

[21] Greß T, Glück Nardi V, Schmid S, Hoyer J, Rizaiev Y, Boll T, et al. Vertical continuous compound casting of copper aluminum bilayer rods. J Mater Process Technol 2021;288:116854. http://dx.doi.org/10.1016/j.jmatprotec.2020.116854.

[22] Choi J, Mazumder J. Numerical and experimental analysis for solidification and residual stress in the GMAW process for AISI 304 stainless steel. J Mater Sci 2002;37:2143–58. http://dx.doi.org/10.1023/A:1015258322780.

[23] Capriccioli A, Frosi P. Multipurpose ANSYS FE procedure for welding processes simulation. Fusion Eng Des 2009;84(2–6):546–53. http://dx.doi.org/10.1016/j.fusengdes.2009.01.039.

[24] Bhatti AA, Barsoum Z, Murakawa H, Barsoum I. Influence of thermo-mechanical material properties of different steel grades on welding residual stresses and angular distortion. Mater Des 2015;65:878–89. http://dx.doi.org/10.1016/j.matdes.2014.10.019.

[25] Hemmesi K, Farajian M, Boin M. Numerical studies of welding residual stresses in tubular joints and experimental validations by means of x-ray and neutron diffraction analysis. Mater Des 2017;126:339–50. http://dx.doi.org/10.1016/j.matdes.2017.03.088.

[26] Majidi HR, Torabi AR, Zabihi M, Razavi SM, Berto F. Energy-based ductile failure predictions in cracked friction-stir welded joints. Eng Fail Anal 2019;102:327–37. http://dx.doi.org/10.1016/j.engfailanal.2019.04.066.

[27] Xin H, Veljkovic M. Residual stress effects on fatigue crack growth rate of mild steel S355 exposed to air and seawater environments. Mater Des 2020;193:108732. http://dx.doi.org/10.1016/j.matdes.2020.108732.

[28] Chen J, Salvati E, Uzun F, Papadaki C, Wang Z, Everaerts J, et al. An experimental and numerical analysis of residual stresses in a TIG weldment of a single crystal nickel-base superalloy. J Manuf Process 2020;53:190–200. http://dx.doi.org/10.1016/j.jmapro.2020.02.007.

[29] Hemmesi K, Mallet P, Farajian M. Numerical evaluation of surface welding residual stress behavior under multiaxial mechanical loading and experimental validations. Int J Mech Sci 2020;168:105127. http://dx.doi.org/10.1016/j.ijmecsci.2019.105127.

[30] Lee JH, Jang BS, Kim HJ, Shim SH, Im SW. The effect of weld residual stress on fracture toughness at the intersection of two welding lines of offshore tubular structure. Mar Struct 2020;71:102708. http://dx.doi.org/10.1016/j.marstruc.2020.102708.

[31] Asadi P, Alimohammadi S, Kohantorabi O, Fazli A, Akbari M. Effects of material type, preheating and weld pass number on residual stress of welded steel pipes by multi-pass TIG welding (C-Mn, SUS304, SUS316). Therm Sci Eng Prog 2020;16:100462. http://dx.doi.org/10.1016/j.tsep.2019.100462.

[32] Lin J, Ma N, Liu X, Lei Y. Modification of residual stress distribution in welded joint of titanium alloy with multi electron beam heating. J Mater Process Technol 2020;278:116504. http://dx.doi.org/10.1016/j.jmatprotec.2019.116504.

[33] Ansaripour N, Heidari A, Eftekhari SA. Multi-objective optimization of residual stresses and distortion in submerged arc welding process using genetic algorithm and harmony search. Proc Inst Mech Eng C J Mech Eng Sci 2020;234(4):862–71. http://dx.doi.org/10.1177/0954406219885977.

[34] Lu Y, Zhu S, Zhao Z, Chen T, Zeng J. Numerical simulation of residual stresses in aluminum alloy welded joints. J Manuf Process 2020;50:380–93. http://dx.doi.org/10.1016/j.jmapro.2019.12.056.

[35] An K, Yuan L, Dial L, Spinelli I, Stoica AD, Gao Y. Neutron residual stress measurement and numerical modeling in a curved thin-walled structure by laser powder bed fusion additive manufacturing. Mater Des 2017;135:122–32. http://dx.doi.org/10.1016/j.matdes.2017.09.018.

[36] Schnabel K, Baumgartner J, Möller B. Fatigue assessment of additively manufactured metallic structures using local approaches based on finite-element simulations. Procedia Struct Integr 2019;19:442–51. http://dx.doi.org/10.1016/j.prostr.2019.12.048.

[37] Bertini L, Bucchi F, Frendo F, Moda M, Monelli BD. Residual stress prediction in selective laser melting: A critical review of simulation strategies. Int J Adv Manuf Technol 2019;105(1–4):609–36. http://dx.doi.org/10.1007/s00170-019-04091-5.

[38] Moda M. Modeling of powder bed fusion additive manufacturing (Ph.D. thesis), University of Pisa; 2020, p. 148. http://dx.doi.org/10.13131/etd/03092021-124517.

[39] Wagener R, Hell M, Scurria M, Bein T. Deriving the structural fatigue behavior of additively manufactured components. In: Minerals, metals and materials series. Springer; 2020, p. 139–49. http://dx.doi.org/10.1007/978-3-030-36296-6_13.

[40] Razavi SM, Van Hooreweder B, Berto F. Effect of build thickness and geometry on quasi-static and fatigue behavior of Ti-6Al-4V produced by electron beam melting. Addit Manuf 2020;36:101426. http://dx.doi.org/10.1016/j.addma.2020.101426.

[41] Goldak J, Chakravarti A, Bibby M. A new finite element model for welding heat sources. Metall Trans B 1984;15(2):299–305. http://dx.doi.org/10.1007/BF02667333.

[42] Kik T. Heat source models in numerical simulations of laser welding. Materials 2020;13(11):2653. http://dx.doi.org/10.3390/ma13112653.

[43] Ferro P, Berto F. Quantification of the influence of residual stresses on fatigue strength of al-alloy welded joints by means of the local strain energy density approach. Strength Mater 2016;48:426–36. http://dx.doi.org/10.1007/s11223-016-9781-0.

[44] Chiocca A, Frendo F, Bertini L. Evaluation of residual stresses in a pipe-to-plate welded joint by means of uncoupled thermal-structural simulation and experimental tests. Int J Mech Sci 2021;199:106401. http://dx.doi.org/10.1016/j.ijmecsci.2021.106401.

[45] Chiocca A, Frendo F, Bertini L. Evaluation of heat sources for the simulation of the temperature distribution in gas metal arc welded joints. Metals 2019;9(11):1142. http://dx.doi.org/10.3390/met9111142.

[46] Chiocca A, Frendo F, Bertini L. Evaluation of residual stresses in a tube-to-plate welded joint. MATEC Web Conf 2019;300:19005. http://dx.doi.org/10.1051/matecconf/201930019005.

[47] Bertini L, Cera A, Frendo F. Experimental investigation of the fatigue resistance of pipe-to-plate welded connections under bending, torsion and mixed mode loading. Int J Fatigue 2014;68:178–85. http://dx.doi.org/10.1016/j.ijfatigue.2014.05.005.

[48] Frendo F, Bertini L. Fatigue resistance of pipe-to-plate welded joint under in-phase and out-of-phase combined bending and torsion. Int J Fatigue 2015;79:46–53. http://dx.doi.org/10.1016/j.ijfatigue.2015.04.020.

[49] Bertini L, Frendo F, Marulo G. Effects of plate stiffness on the fatigue resistance and failure location of pipe-to-plate welded joints under bending. Int J Fatigue 2016;90:78–86. http://dx.doi.org/10.1016/j.ijfatigue.2016.04.015.

[50] Frendo F, Marulo G, Chiocca A, Bertini L. Fatigue life assessment of welded joints under sequences of bending and torsion loading blocks of different lengths. Fatigue Fract Eng Mater Struct 2020;43(6):1290–304. http://dx.doi.org/10.1111/ffe.13223.

[51] Chiocca A, Frendo F, Bertini L. Experimental evaluation of relaxed strains in a pipe-to-plate welded joint by means of incremental cutting process. Procedia Struct Integr 2020;28:2157–67. http://dx.doi.org/10.1016/j.prostr.2020.11.043.

[52] Lopez Z, Fatemi A. A method of predicting cyclic stress-strain curve from tensile properties for steels. Mater Sci Eng A 2012;556:540–50. http://dx.doi.org/10.1016/j.msea.2012.07.024.

[53] Hemmesi K, Farajian M, Fatemi A. Application of the critical plane approach to the torsional fatigue assessment of welds considering the effect of residual stresses. Int J Fatigue 2017;101:271–81. http://dx.doi.org/10.1016/j.ijfatigue.2017.01.023.

[54] Kang G, Luo H. Review on fatigue life prediction models of welded joint. Acta Mech Sinica 2020;36:701–26. http://dx.doi.org/10.1007/s10409-020-00957-0.

[55] Andrianopoulos NP, Pikrakis A. On the effect of hydrostatic stress on fatigue crack propagation. Int J Struct Integr 2017;8(2):240–55. http://dx.doi.org/10.1108/IJSI-06-2016-0021.

[56] Qilafku G, Kadi N, Dobranski J, Azari Z, Gjonaj M, Pluvinage G. Fatigue of specimens subjected to combined loading. Role of hydrostatic pressure. Int J Fatigue 2001;23(8):689–701. http://dx.doi.org/10.1016/S0142-1123(01)00030-5.

[57] Kondori B, Benzerga AA. Effect of stress triaxiality on the flow and fracture of Mg alloy AZ31. Metall Mater Trans A Phys Metall Mater Sci 2014;45:3292–307. http://dx.doi.org/10.1007/s11661-014-2211-7.

[58] Crossland B. Effect of large hydrostatic pressures on the torsional fatigue strength of an alloy steel. In: Proceedings of the international conference on fatigue of metals. 1956, p. 138–49.

[59] Burns DJ, Parry JSC. Effect of large hydrostatic pressures on the torsional fatigue strength of two steels. J Mech Eng Sci 1964;6(3):293–310. http://dx.doi.org/10.1243/jmes_jour_1964_006_042_02.

[60] Standard A. ASTM E92-16 Standard test methods for vickers hardness and knoop hardness of metallic. Am Soc Test Mater 2016;82:1–27.

[61] Wang X, Shao C, Liu X, Lu F. Transition and fracture shift behavior in LCF test of dissimilar welded joint at elevated temperature. J Mater Sci Technol 2018;34(4):720–31. http://dx.doi.org/10.1016/j.jmst.2017.06.015.

[62] Rao TE, Krishna GR, Kumar MV. Investigation of microstructure and mechanical properties of MIG welded mild steel plates. Ann Chimie Sci Materiaux 2019;43(4):257–63. http://dx.doi.org/10.18280/acsm.430409.

[63] Wan Muda WSH, Mohd Nasir NS, Mamat S, Jamian S. Effect of welding heat input on microstructure and mechanical properties at coarse grain heat affected zone of ABS grade a steel. ARPN J Eng Appl Sci 2015;10(20):9487–95.

[64] Dudziński W, Konat Ł, Pękalski G. Structural and strength characteristics of wear-resistant martensitic steels. Arch Foundry Eng 2008;8(2):21–6.

[65] Wang Y, Li L. Microstructure evolution of fine-grained heat-affected zone in type IV failure of P91 welds. Weld J 2016;95(1):27s–36s.

[66] Harris J. Engineering metallurgy: Part 1 applied physical metallurgy. Int Mater Rev 1994;39(5):213–4. http://dx.doi.org/10.1179/imr.1994.39.5.213.

[67] Hollomon J, Jaffe L. Time-temperature relations in tempering steels. Trans Am Inst Min Metall Eng 1945;162:223–49.

[68] Grange RA, Hribal CR, Porter LF. Hardness of tempered martensite in carbon and low-alloy steels. Metall Trans A 1977;8 A(11):1775–85. http://dx.doi.org/10.1007/BF02646882.

[69] Radaj D, Sonsino CM, Fricke W. Fatigue assessment of welded joints by local approaches. 2nd ed.. 2006, p. 1–639. http://dx.doi.org/10.1533/9781845691882.

[70] Taylor D. The theory of critical distances. Eng Fract Mech 2008;75(7):1696–705. http://dx.doi.org/10.1016/j.engfracmech.2007.04.007.

[71] Meneghetti G. The peak stress method for fatigue strength assessment of tube-to-flange welded joints under torsion loading. Weld World 2013;57(2):265–75. http://dx.doi.org/10.1007/s40194-013-0022-x.

[72] Meneghetti G, Campagnolo A, Visentin A, Avalle M, Benedetti M, Bighelli A, et al. Rapid evaluation of notch stress intensity factors using the peak stress method with 3D tetrahedral finite element models: Comparison of commercial codes. Fatigue Fract Eng Mater Struct 2022;45(4):1005–34. http://dx.doi.org/10.1111/ffe.13645.

[73] Zhu J, Khurshid M, Barsoum Z. Accuracy of computational welding mechanics methods for estimation of angular distortion and residual stresses. Weld World 2019;63:1391–405. http://dx.doi.org/10.1007/s40194-019-00746-9.

[74] Cho SH, Kim JW. Analysis of residual stress in carbon steel weldment incorporating phase transformations. Sci Technol Weld Join 2002;7(4):212–6. http://dx.doi.org/10.1179/136217102225004257.

[75] Deng D. FEM Prediction of welding residual stress and distortion in carbon steel considering phase transformation effects. Mater Des 2009;30(2):359–66. http://dx.doi.org/10.1016/j.matdes.2008.04.052.

[76] Caprace JD, Fu G, Carrara JF, Remes H, Shin SB. A benchmark study of uncertainness in welding simulation. Mar Struct 2017;56:69–84. http://dx.doi.org/10.1016/j.marstruc.2017.07.005.